Supplementary Information (SI) for New Journal of Chemistry.

Supporting Information

Various White MOFs-based Cryogels for Passive Daytime Radiative Cooling

Haotian Gao[a], Xiao-Min Li[a,], Huan Wu[a], Junkuo Gao[a,b,]**

[a]China-Uzbekistan Joint Laboratory on Advanced Porous Materials, State Key Laboratory of Bio-based Fiber Materials, School of Materials Science and Engineering, Zhejiang Sci-Tech University, Hangzhou 310018, China.

[b]State Key Laboratory of Organic Electronics and Information Displays & Institute of Advanced Materials (IAM), Nanjing University of Posts & Telecommunications, Nanjing 210023, China

AUTHOR INFORMATION

Corresponding Authors: lixm@zstu.edu.cn (Xiao-Min Li)**;** jkgao@zstu.edu.cn (Junkuo Gao)

Materials

Piperazine anhydrous, phosphorous acid (H_3PO_3), fumaric acid, Potassium hydroxide (KOH), Zirconium oxychloride octahydrate ($ZrOCl_2 \cdot 8H_2O$), and anhydrous formic acid (HCOOH) were purchased from Shanghai Maclean Biochemical Technology Co., Ltd. Aluminum acetylacetonate, 2-methylimidazole, sodium hydroxide (NaOH, 98 %), terephthalic acid (H_2BDC) were obtained from Anhui Zesheng Technology Co., Ltd. Titanium oxyacetylacetonate was bought from Bide Pharmatech Co., Ltd. (China). Zinc nitrate hexahydrate ($Zn(NO_3)_2 \cdot 6H_2O$) was supplied from Sinopharm Chemical Reagent Co., Ltd. (China). Hydrochloric acid (HCl) was purchased from Huzhou Shuanglin Chemical Technology Co., Ltd. Formaldehyde (CH_2O), aluminum sulfate octadecahydrate ($Al_2(SO_4)_3 \cdot 18H_2O$), and polyvinyl alcohol (PVA) were obtained from Aladdin Reagent Co., Ltd. Methanol, anhydrous ethanol, N, N-dimethylformamide (DMF) were obtained from Hangzhou Gaojing Fine Chemical Co. Ltd. All reagents were used without further purification.

Preparations of the ligand of MIL-91

The ligand N, N'-piperazinebis (methylene phosphonic acid) was synthesized from a modified Mannich reaction.[1] A mixture of hydrochloric acid (10 mL, 37 wt%) and water (10 mL) was added to piperazine (6.89 g, 0.08 mol) and phosphorous acid (17.06 g, 0.21 mol) to form a colorless solution, which was then refluxed (1 hour). Formaldehyde (20 mL, 37 wt%) was added drop wise over a 2-hour period to form a white suspension. After refluxing for 24 hours, the reaction was cooled and the solvent volume reduced by 70% under vacuum. An ethanol-water (9:1, 40 mL) solution was added to the product and refrigerated overnight to precipitate any remaining ligand. The product was collected by filtration, washed with an ethanol-water (9:1, 2 × 30 mL) solution and dried (90 °C, overnight) to afford a white powder.

Preparations of the MIL-91(Al)

The synthesis of MIL-91(Al) was based on a previous report.[2] 1.14 g of ligand (4.17 mmol) was weighed, poured into a 50 mL beaker, and 30 mL of deionized water was added to dissolve it; the pH of the solution was adjusted to ~5 with 1 M aqueous NaOH, and it was transferred to a 500 mL round-bottomed flask and stirred at 333 K for 30 min. Then 1.80 g aluminum acetylacetonate (5.55 mmol) was added to the flask for subsequent refluxing process of 88 h. The solution was then purified by filtration of 20 mL of water. At the end of the reflux process, the precipitate with MIL-91(Al) as the only crystalline phase was cooled and washed three times by filtration with 20 mL of water. Finally, the product was dried at 80 °C for 12 h. The synthesized product was stored for further analysis and application.

Preparations of the MIL-91(Ti)

The synthesis of MIL-91(Al) was based on a previous report.[1] 1.14 g of ligand (4.17 mmol) was weighed, poured into a 50 mL beaker, and 30 mL of deionized water was added to dissolve it; the pH of the solution was adjusted to ~5 with 1 M aqueous NaOH, and it was transferred to a 500 mL round-bottomed flask and stirred at 333 K for 30 min. Then 1.09 g titanium oxyacetylacetonate (4.17 mmol) was added to the flask for subsequent refluxing process of 40 h. The solution was then purified by filtration of 20 mL of water. At the end of the reflux process, the precipitate with MIL-91(Ti) as the only crystalline phase was cooled and washed three times by filtration with 20 mL of water. Finally, the product was dried at 80 °C for 12 h. The synthesized product was stored for further analysis and application.

Preparation of AlFu

The synthesis of MIL-91(Al) was based on a previous report.[3] 39.96 g of $Al_2(SO_4)_3 \cdot 18H_2O$ was dissolved in 400 mL of deionized water, which was recorded as solution A. 13.92 g of fumaric acid and 20.16 g of KOH were dissolved in 400 mL of deionized water, which was recorded as solution B. After the two solutions A and B were fully dissolved, solution B was poured into solution A to obtain a milky white solution, and the oil bath was carried out at 80 °C for 3 h. After the reaction was completed, the solution was waited to cool down to room temperature, and the white powder cake was obtained by pumping and filtering, and it was washed with deionized water for several times. Finally, the product was dried at 60 °C for 12 h. The synthesized product was stored for further analysis and application.

Preparation of UiO-66

The synthesis of MIL-91(Al) was based on a previous report.[4] 17 g of $ZrOCl_2·8H_2O$ was dissolved in 100 mL of DMF to which 100 mL of DMF solution containing 8.3 g of H_2BDC was subsequently added to form a mixed solution. To the mixed solution was added 100 mL of anhydrous formic acid (98%), followed by condensation reflux at 120 °C for 4 h. At the end of the reaction, it was filtered and washed with DMF and methanol three times each. Finally, the product was dried at 60 °C for 24 h. The synthesized product was stored for further analysis and application.

Preparation of ZIF-8

The synthesis of MIL-91(Al) was based on a previous report.[5] 13.14g of 2-methylimidazole was dissolved in 150 mL of methanol, which was recorded as solution A. 11.90 g of $Zn(NO_3)_2·6H_2O$ was dissolved in 300 mL of methanol, which was recorded as solution B. After sonication of each of the solutions A and B for 30 min until all of them were dissolved, the solution A was quickly added to the solution B, stirred for 1 h, and then left to stand for 24 h under the water bath at 30 °C, so that crystals would be precipitated continuously. After waiting for the end of the stationary period, the supernatant was poured off, and then the remaining white solution was centrifuged (8000 rpm, 3 min) and washed with methanol for three times. Finally, the product was dried at 60 °C for 12 h. The synthesized product was stored for further analysis and application.

Preparation of MOF-based cryogels

Polyvinyl alcohol (PVA) was dissolved in the deionized water with the ratio of 1:10 by mass/volume at 85 °C. The mixture of MOFs (1 g) and PVA solution (2 mL) was added into deionized water (2 mL), and then stirred at a high-speed of 1000 r min^{-1} for 2 hours. After stirring, the obtained product was treated with ultrasonic for defoaming, poured into acrylic mold. The mold was placed in an ice-ethanol bath at -80 °C and then freeze-dried for 48 hours.

Apparatus

The main instruments we use are: the high-speed disperser of model IKA T18 produced by German Aika Company; the ultrasonic cell crusher of model JY92-2D produced by Ningbo Xinzhi Biotechnology Company; the X-ray powder diffractometer of model D8 Advance produced by German Bruker Company; the scanning electron microscope of model GeminiSEM500 produced by German Zeiss Company; the thermogravimetric analyzer of model Pyris Diamond TGA produced by American PE Company; the specific surface area and pore size analyzer of model BSD660M A3M produced by Beijing Beiside Company; the ultraviolet-visible spectrophotometer of model UH4150 produced by American Thermo Electron Corporation; the Fourier transform infrared spectrometer of model Nicolet is 50 produced by American Instron Company; the contact angle measurement instrument of model OCA 15EC produced by German Deif Company; the infrared thermal imager of model H21 PRO produced by Hangzhou Haikang Microimaging Company; the K-type thermocouple of model K-0.5-C produced by China Aidiwen Company; the temperature measurement recorder and The accelerated UV aging tests were performed in a QUV/SPRAY test chamber (Q-LAB Company) in accordance with the standard GB/T 31899—2015. Diffuse reflectance spectra across the ultraviolet-visible-near-infrared (UV-Vis-NIR) range were obtained using a Hitachi UH4150 ultraviolet-visible spectrophotometer, with barium sulfate serving as the reference standard. Additionally, the infrared emissivity of the cryogel was determined using a Thermo Fisher Scientific Nicolet IS50 Fourier transform infrared spectrometer. To elucidate the optical mechanisms underlying the hierarchical porous structure of the cryogels, Finite-Difference Time-Domain (FDTD) simulations were performed using Ansys Lumerical FDTD Solutions. Three-dimensional (3D) models were constructed for numerical analysis. A plane wave source was introduced across the spectral range of 0.25 to 25 μm. Periodic boundary conditions were applied along the x- and y-axes, while perfectly matched layers (PMLs) were used along the z-axis to eliminate boundary reflections. To explore the influence of pore architecture, random nanoporous models (250－1500) nm were established, each with a uniform pore density. As shown in the fig., the simulations reveal enhanced broadband light scattering resulting from the pore design, corroborating the experimental observations of high solar reflectance.AM1.5 indicates that the path of sunlight passing through the atmosphere at this time is 1.5 times that of when it is incident perpendicularly (AM1). It is well known that AM1.5 is indeed the internationally recognized standard solar spectrum used for testing and efficiency calibration of ground-based photovoltaic devices. Due to the different positions where sunlight reaches the earth, different latitudes, the amount of sunlight radiation received by the Earth varies at any given time. When the sun is not directly overhead, the light passes through the atmosphere at an inclined angle, and the path becomes longer. It includes direct sunlight and scattered sunlight (the diffuse light in the sky). At a solar zenith angle of 48.2, the total irradiance is approximately 1000 W/m². Therefore, for the convenience of research, people proposed to use AM1.5 (ASTM G173-03) to represent the standard solar spectrum.

Under clear skies, atmospheric radiation is the result of the interaction of different radiation sources. For instance, many gases in the atmosphere, such as nitrogen (N_2), oxygen (O_2), water vapor (H_2O), etc, act as semi-transparent diffusers. Due to their low transmittance, the thermal radiation from the Earth's surface to outer space is weakened. Under the combined effect of various atmospheric components, an optimal atmospheric radiation wavelength range of 8 to 13 μm is formed, known as the "atmospheric window", which has a very high transparency in this band. The transmittance of the atmospheric window is influenced by various factors, such as geographical location, cloud cover, zenith angle, and atmospheric humidity, etc. In this article, we used the Modtran5 software to simulate the atmospheric windows.

Definition of Solar Reflectance, Thermal Emittance and Cooling Power of MOF-Based Cryogels

To achieve passive daytime radiative cooling, an object must minimize radiative heat gain from the sun and maximize radiative heat loss to the cold sky above. The first implies that the surface must have a high solar reflectance $R_{(solar)}$, defined as:

$$R(solar) = \frac{\int_{\lambda 1}^{\lambda 2} I(\lambda)R(\lambda)d\lambda}{\int_{\lambda 1}^{\lambda 2} I(\lambda)d\lambda} \quad (1)$$

Where λ is the wavelength, I (λ) is the ASTM G173 Global solar intensity spectrum, and R (λ) is the sample surface's spectral reflectance. $\lambda_1 = 0.3$ μm and $\lambda_2 = 2.5$ μm.

To maximize thermal emission into the sky, the surface must have a high hemispherical LWIR emittance ϵ_{LWIR}, defined as:

(2)

$$\epsilon LWIR = \frac{\int_{\lambda 1}^{\lambda 2} IBB(T,\lambda)\varepsilon(T,\lambda)d\lambda}{\int_{\lambda 1}^{\lambda 2} IBB(T,\lambda)d\lambda}$$

where the 8-13 µm bounds represent the LWIR atmospheric transmittance window, I_{BB} (T, λ) is the spectral intensity emitted by a blackbody at temperature T (assumed to be 25°C) and ϵ (T, λ) is the sample surface's spectral hemispherical thermal emittance. λ_1 =8 µm and λ_2 = 13 µm.

The daytime cooling power of a radiative cooler is calculated by the following equation:

$$PCooling = Prad(T) - Psolar - Patm(Tamb) - Pnon - rad \tag{3}$$

where Prad (T) represents the power radiated out by the radiative cooler at temperature T, which can be defined as:

$$Prad(T) = 2\pi \int_{0}^{\frac{\pi}{2}} \sin\theta \cos\theta d\theta \int_{2.5\mu m}^{25\mu m} IBB(T,\lambda)\varepsilon(\lambda)d\lambda \tag{4}$$

$$IBB(T,\lambda) = \frac{2hc^2}{\lambda^5} \frac{1}{e^{hc/\lambda kT} - 1} \tag{5}$$

where ε (λ,) is the spectral and angular emissivity of the cooler. h is Planck's constant, k is Boltzmann constant, and c is the speed of light. Atmospheric thermal radiation absorbed by the radiative cooler can be calculated as follows:

$$Patm(Tamb) = 2\pi \int_{0}^{\frac{\pi}{2}} \sin\theta \cos\theta d\theta \int_{2.5\mu m}^{25\mu m} IBB(T,\lambda)\varepsilon(\lambda)\varepsilon atm(\lambda)d\lambda \tag{6}$$

where T_{amb} is the ambient temperature, ε_{atm} (λ) is the spectral and angular emissivity of the atmosphere, which can be defined as ε_{atm} (λ) = 1-t_{atm}(λ). Here t_{atm}(λ) is the atmospheric transmittance in the zenith direction, which can be calculated with Modtran5 for a zenith path from sea level to space through a 1976 US Standard Atmosphere model.

The solar irradiance absorbed by cooler (P_{solar}) and the non-radiative power lost ($P_{non\text{-}rad}$) due to convection and conduction is defined as:

$$Psolar = \int_{0.3\mu m}^{2.5\mu m} Isolar(\lambda)\epsilon(\lambda,\theta)d\lambda \tag{7}$$

$$Pnon - rad = hc(Tamb - T) \tag{8}$$

where h_c is the coefficient of the non-radiative heat.

AM1.5 indicates that the path of sunlight passing through the atmosphere at this time is 1.5 times that of when it is incident perpendicularly (AM1). It is well known that AM1.5 is indeed the internationally recognized standard solar spectrum used for testing and efficiency calibration of ground-based photovoltaic devices. Due to the different positions where sunlight reaches the earth, different latitudes, the amount of sunlight radiation received by the Earth varies at any given time. When the sun is not directly overhead, the light passes through the atmosphere at an inclined angle, and the path becomes longer. It includes direct sunlight and scattered sunlight (the diffuse light in the sky). At a solar zenith angle of 48.2, the total irradiance is approximately 1000 W/m². Therefore, for the convenience of research, people proposed to use AM1.5 (ASTM G173-03) to represent the standard solar spectrum. Under clear skies, atmospheric radiation is the result of the interaction of different radiation sources. For instance, many gases in the atmosphere, such as nitrogen (N_2), oxygen (O_2), water vapor (H_2O), etc, act as semi-transparent diffusers. Due to their low transmittance, the thermal radiation from the Earth's surface to outer space is weakened. Under the combined effect of various atmospheric components, an optimal atmospheric radiation wavelength range of 8 to 13 μm is formed, known as the "atmospheric window", which has a very high transparency in this band. The transmittance of the atmospheric window is influenced by various factors, such as geographical location, cloud cover, zenith angle, and atmospheric humidity, etc. In this article, we used the Modtran5 software to simulate the atmospheric windows.

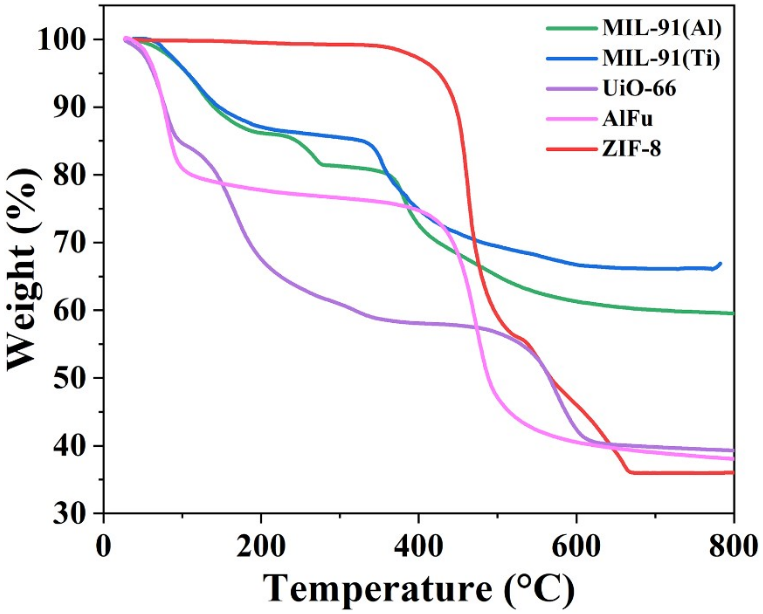

Fig. S1. TGA curves of MOFs.

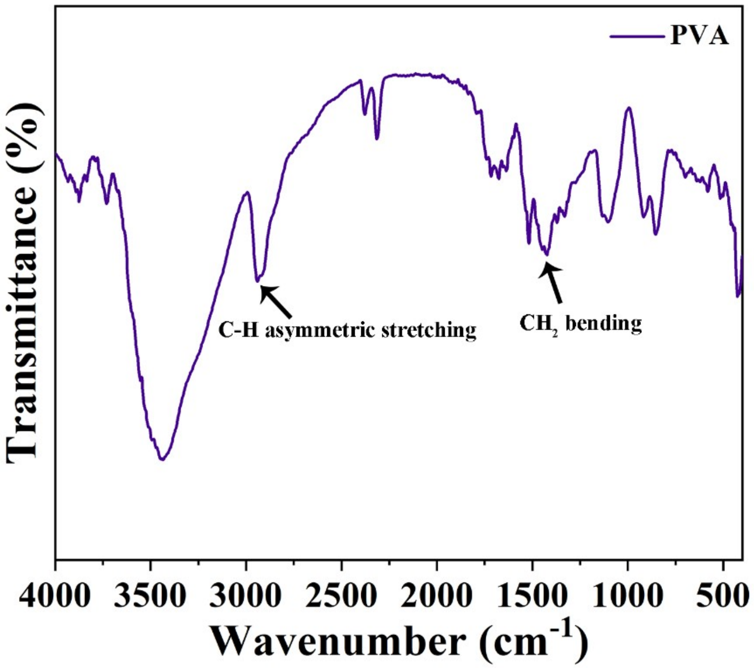

Fig. S2. FT-IR spectrum of PVA.

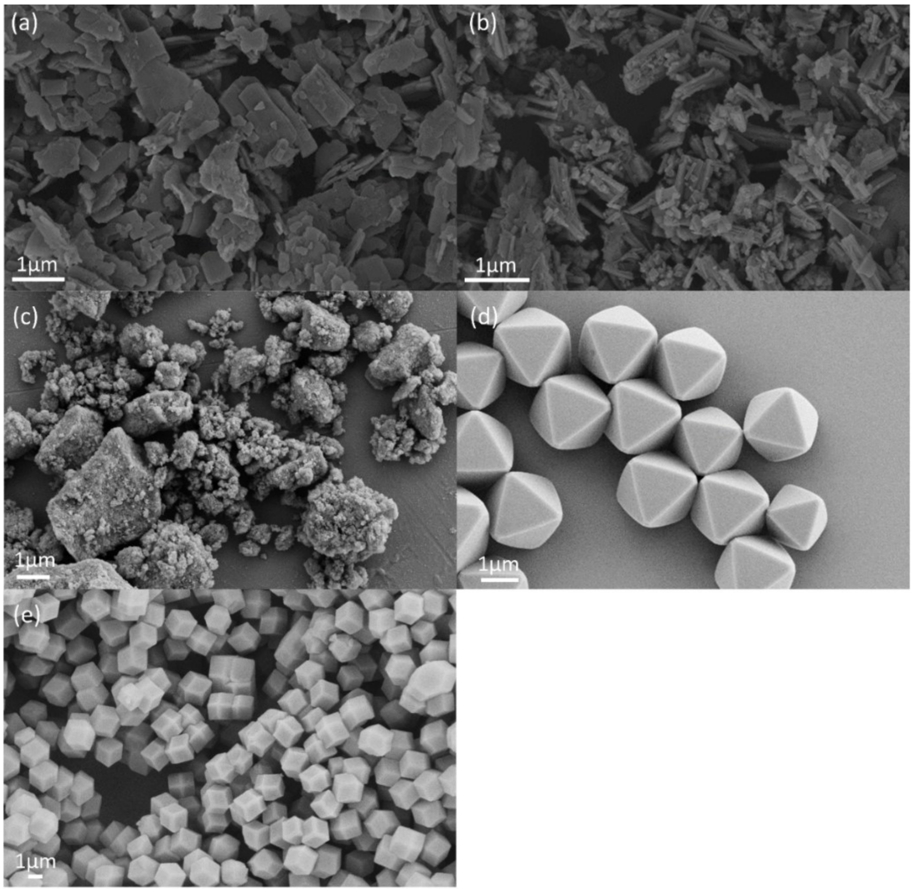

Fig. S3. SEM images of MOFs: (a) MIL-91(Al); (b) MIL-91(Ti); (c) AlFu; (d) UiO-66; (e) ZIF-8.

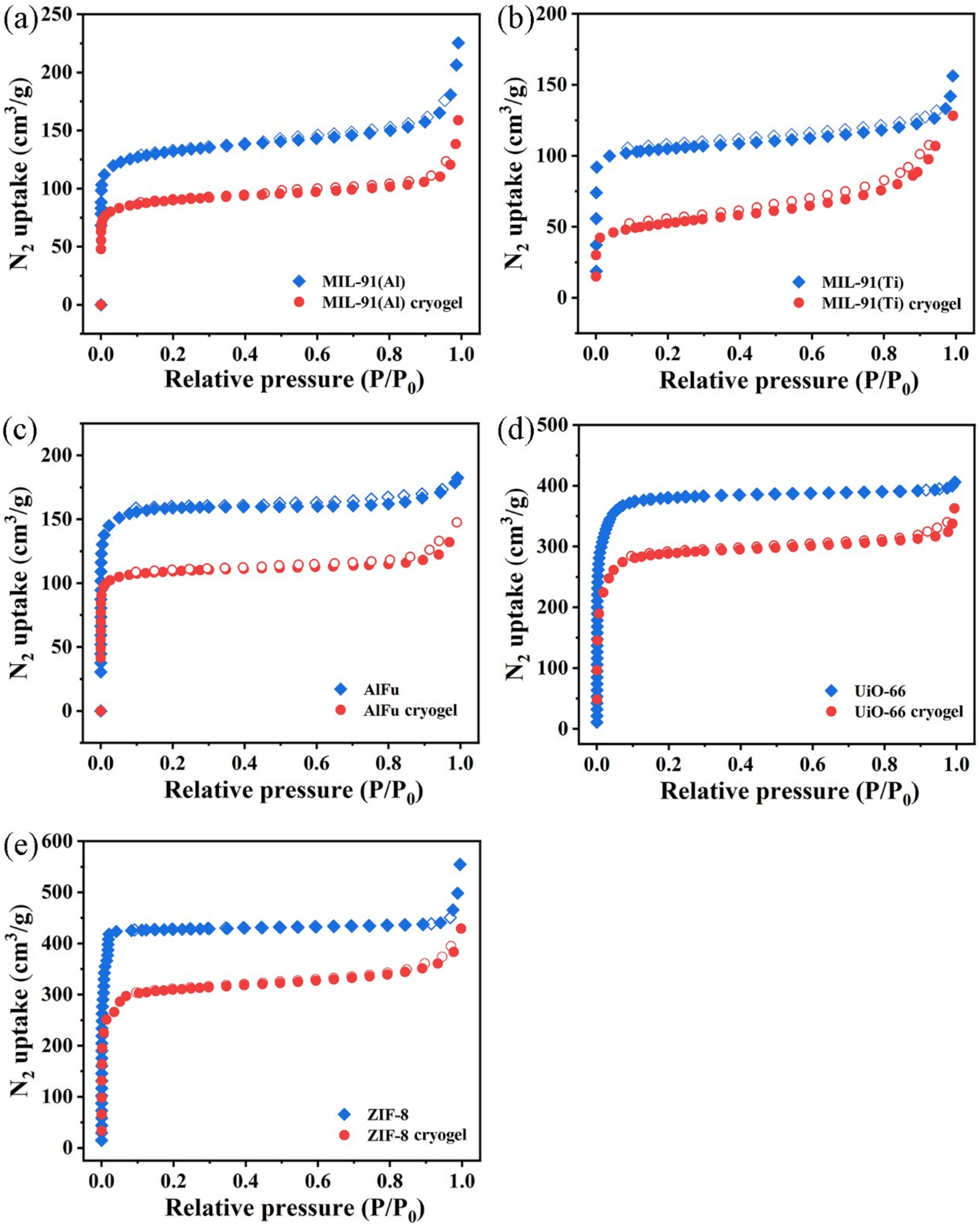

Fig. S4. N_2 adsorption-desorption isotherms measured at 77 K of MIL-91(Al) and MIL-91(Al) cryogel (a), MIL-91(Ti) and MIL-91(Ti) cryogel (b), AlFu and AlFu cryogel (c), UiO-66 and UiO-66 cryogel (d), ZIF-8 and ZIF-8 cryogel (e).

Table S1. The BET surface area, specific pore volume and average pore size for MIL-91(Al), MIL-91(Ti), AlFu, UiO-66, ZIF-8 and their cryogels.

Sample	BET surface area ($m^2 \cdot g^{-1}$)	Pore volume ($cm^3 \cdot g^{-1}$)
MIL-91(Al)	237.4	0.25
MIL-91(Al) cryogel	178.3	0.24
MIL-91(Ti)	313.6	0.24
MIL-91(Ti) cryogel	233.7	0.16
AlFu	688.3	0.28
AlFu cryogel	617.4	0.26
UiO-66	1062.7	0.62
UiO-66 cryogel	824.6	0.33
ZIF-8	1473.6	0.69
ZIF-8 cryogel	1174.9	0.56

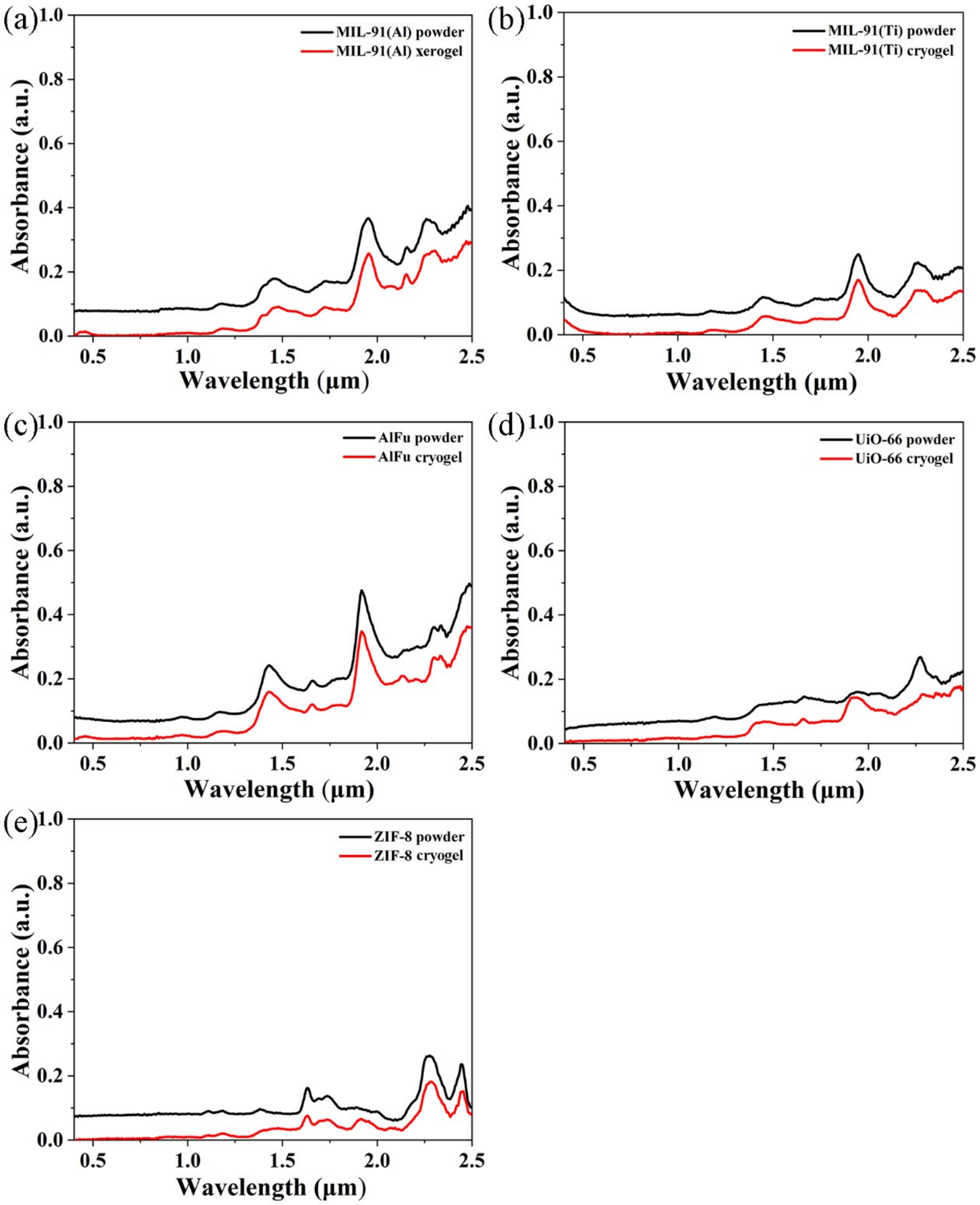

Fig. S5. UV-visible absorption spectra of MOFs and cryogels: (a) MIL-91(Al) and MIL-91(Al) cryogel; (b) MIL-91(Ti) and MIL-91(Ti) cryogel; (c) AlFu and AlFu cryogel; (d) UiO-66 and UiO-66 cryogel.

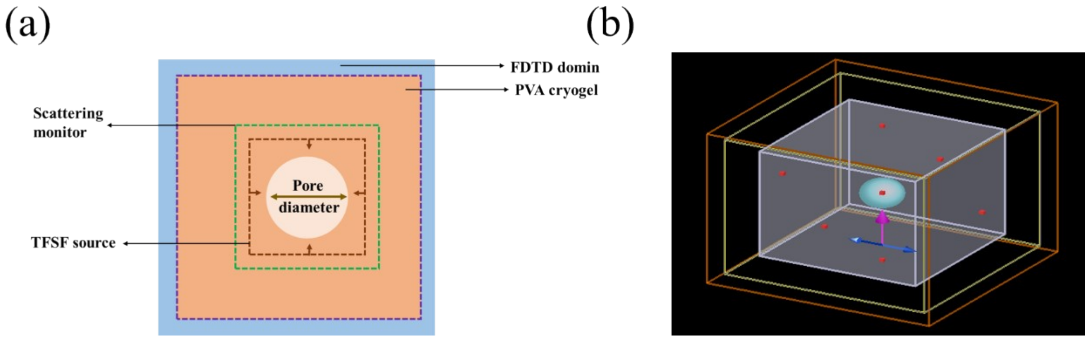

Fig. S6. FDTD-simulated scattering efficiency. (a) Scheme of FDTD simulation scattering efficiency modeling; (b) FDTD-simulation scattering efficiency modeling of 3D images.

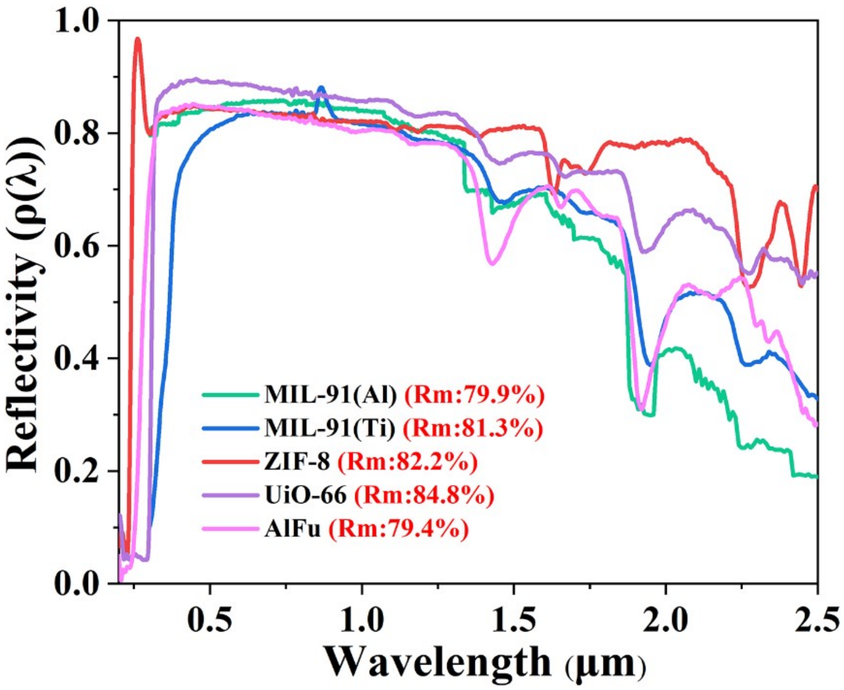

Fig. S7. Reflectance spectra of the MOFs powders against the normalized global solar spectra (ASTM G173).

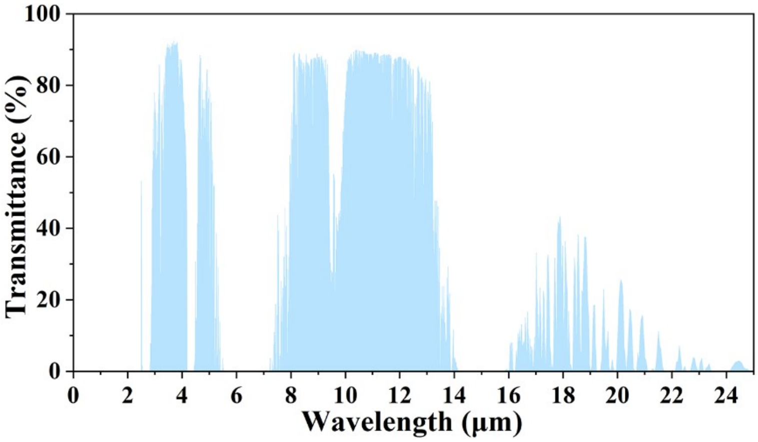

Fig. S8. Atmospheric transmittance versus wavelength (2.5 μm~25 μm), calculated with Modtran5 for a zenith path from sea level to space through a 1976 US Standard Atmosphere model.

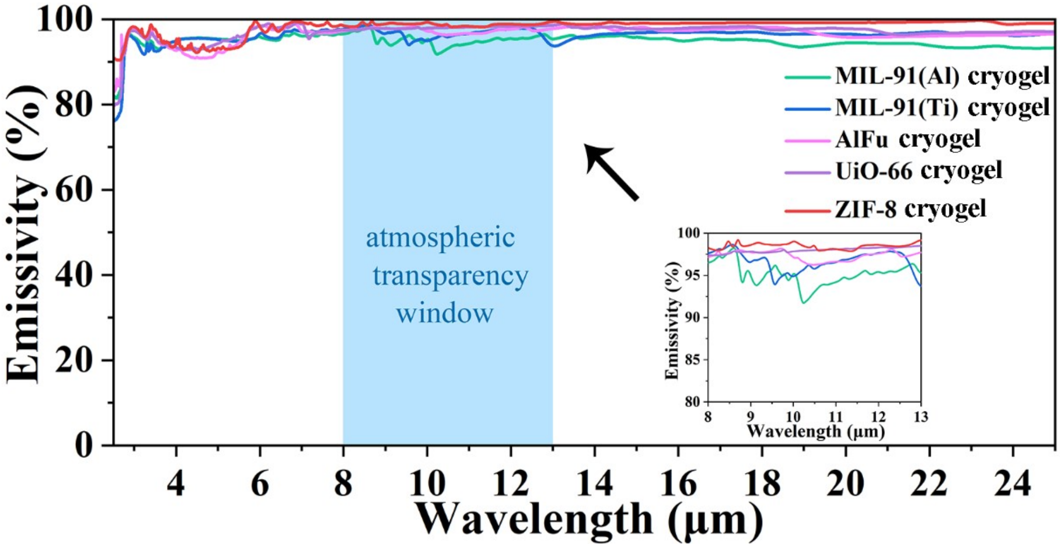

Fig. S9. Emissive spectrum of the MIL-91(Al) cryogel (ε_{LWIR}=95.29%), MIL-91(Ti) cryogel (ε_{LWIR}=95.42%), AlFu cryogel (ε_{LWIR}=96.88%), UiO-66 cryogel (ε_{LWIR}=97.43%) and ZIF-8 cryogel (ε_{LWIR}=97.82%).

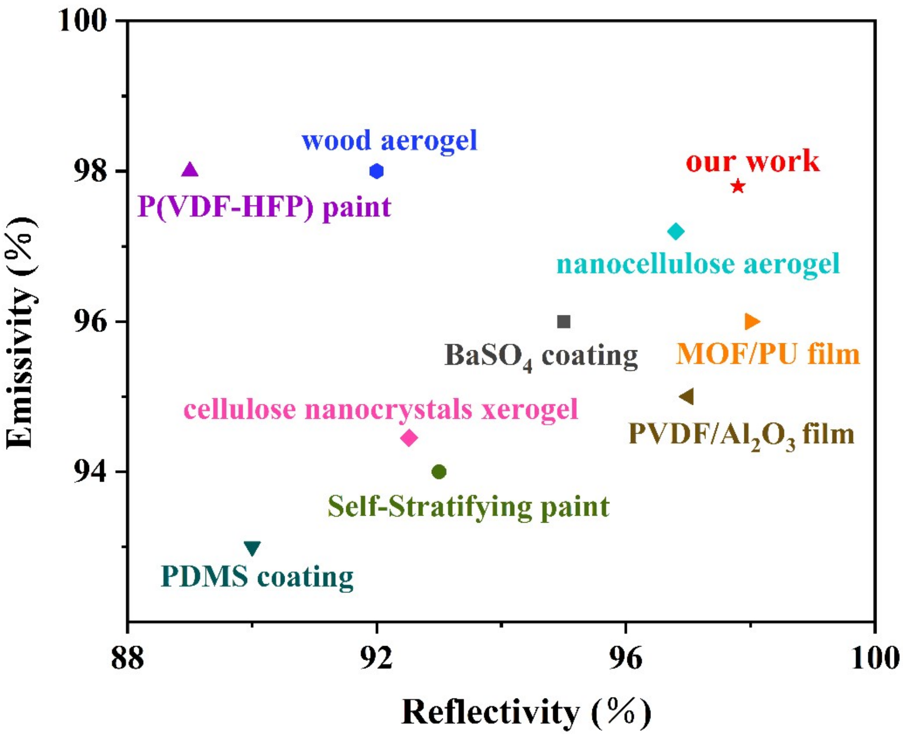

Fig. S10. Comparison of reflectivity and emissivity between the best cryogel (ZIF-8 cryogel) and the previously reported radiation cooling materials ($BaSO_4$ coating,[6] Self-Stratifying Paint,[7] P(VDF-HFP) paint,[8] PDMS coating,[9] nanocellulose cryogel,[10] PVDF/Al_2O_3 film,[11] MOF/PU film,[12] wood cryogel,[13] cellulose nanocrystals xerogel[14]).

Fig. S11. The field optical image of outdoor temperature testing.

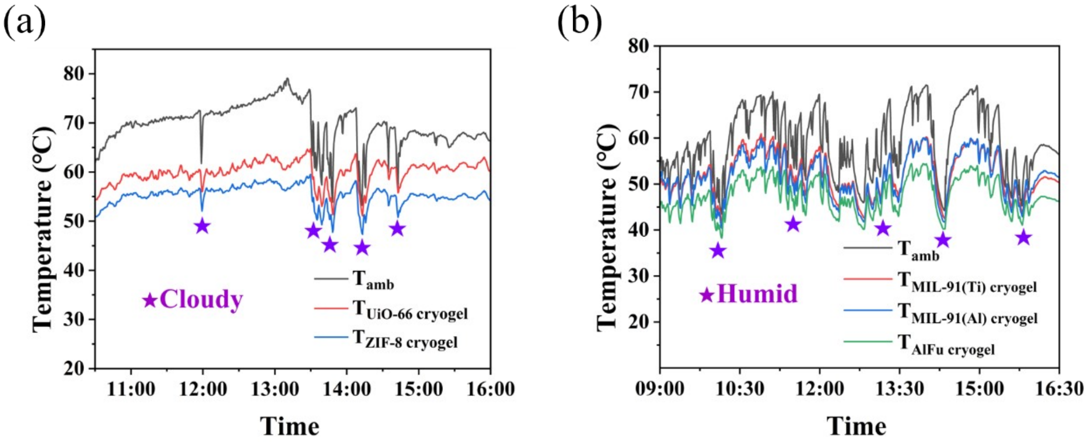

Fig. S12. Outdoor cooling tests of MOFs-based cryogels under different conditions.

Table S2. Performance comparison of MOFs-based cryogel with other materials

Materials	Reflectivity (%)	Emissivity (%)	Cooling effect (℃)	references
ZIF-8 cryogel	97.8	97.8	15.1	This work
Melamine/phytic acid	89.3	90.4	4.3	15
fluorine /silica/functionalized polyimide	92.8	93.0	9.4	16
SiO_2/poly(vinyl alcohol)	93.7	98.19	14.1	17
Wood	92	98	13	18
Cellulose acetate/PVDF-HFP/Al_2O_3	97.4	98.5	8.1	19
PVA/CNF	93	98	8.8	20
PDMS/CNF /nano-SiO_2	93.5	98.5	7.51	21
Paraffin/SiO_2	90	98.7	18.7	22
Rice straw	92.82	95.76	10.8	23

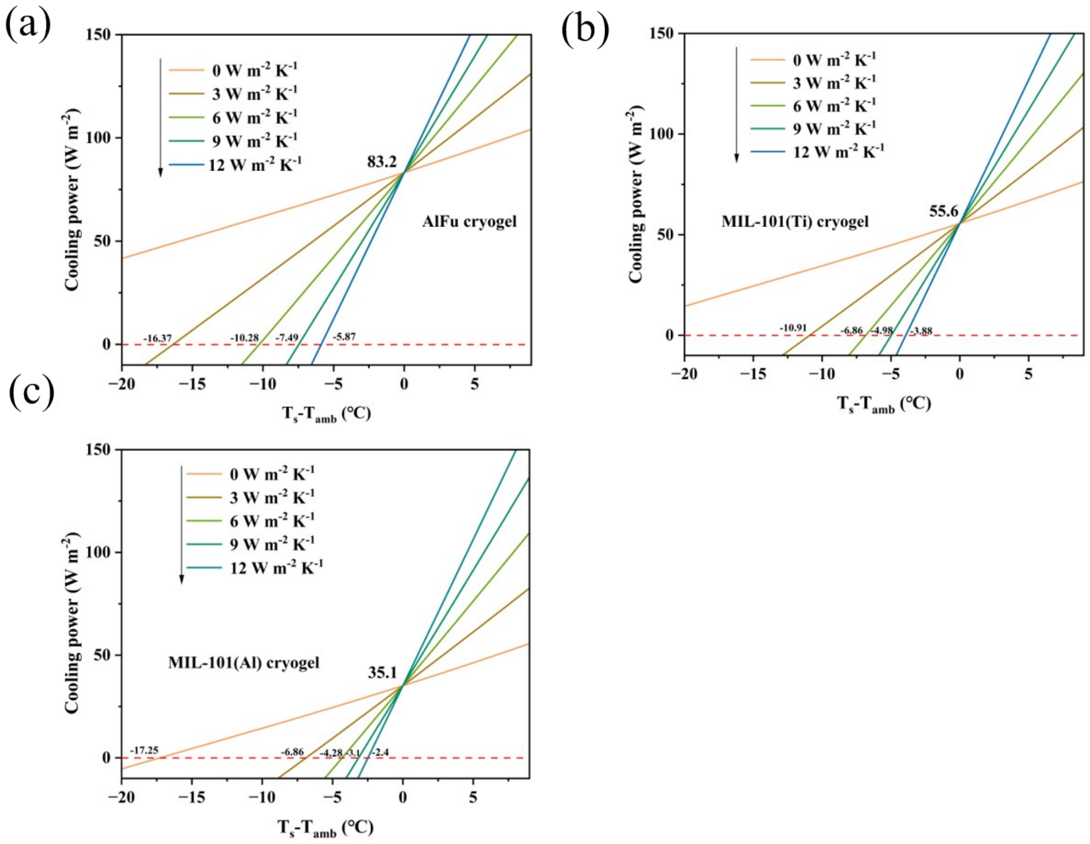

Fig. S13. Calculated net cooling power of others cryogels during the Daytime based on the theoretical passive radiative cooling model. (a) AlFu cryogel; (b) MIL-91(Ti) cryogel; (c) MIL-91(Ti) cryogel.

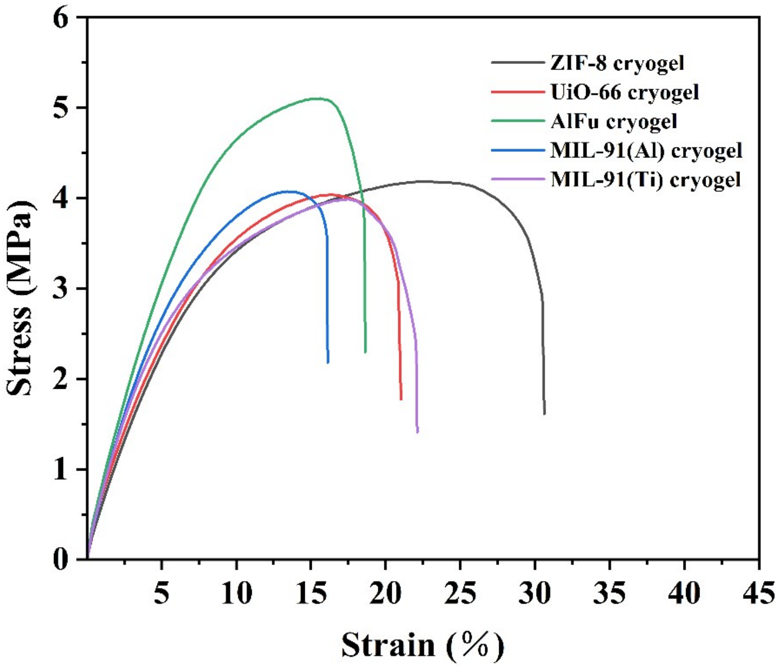

Fig. S14. Stress-strain curves during the stretching process of the MOFs-based cryogels.

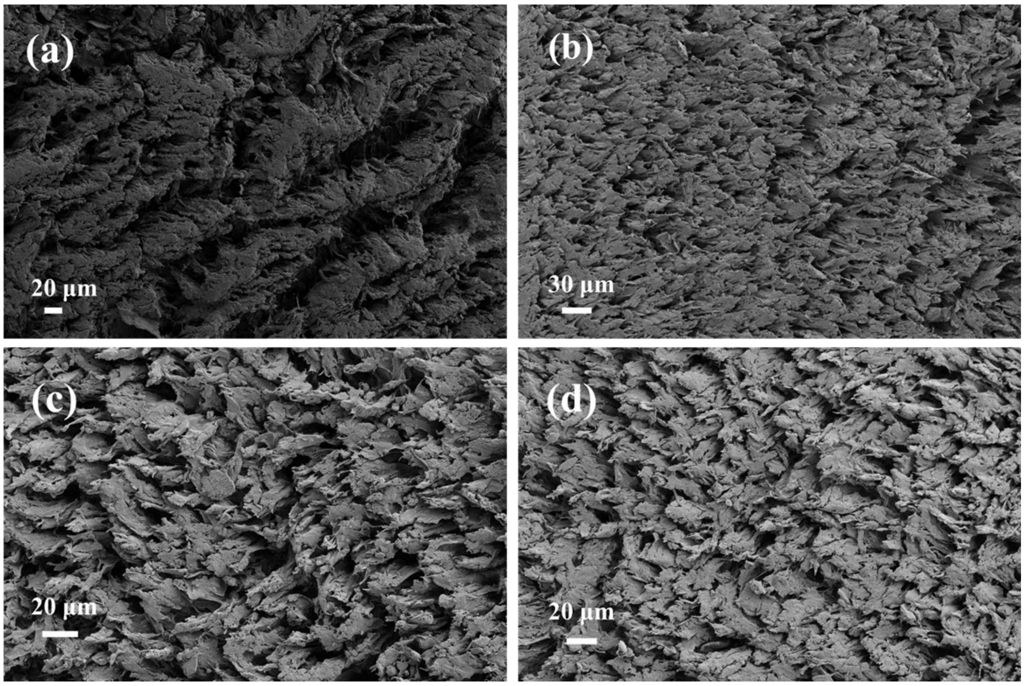

Fig. S15. SEM images of MOF-based cryogels after ultraviolet light aging. (a) UiO-66 cryogel; (b) AlFu cryogel; (c) MIL-91(Al) cryogel; (d) MIL-91(Ti) cryogel

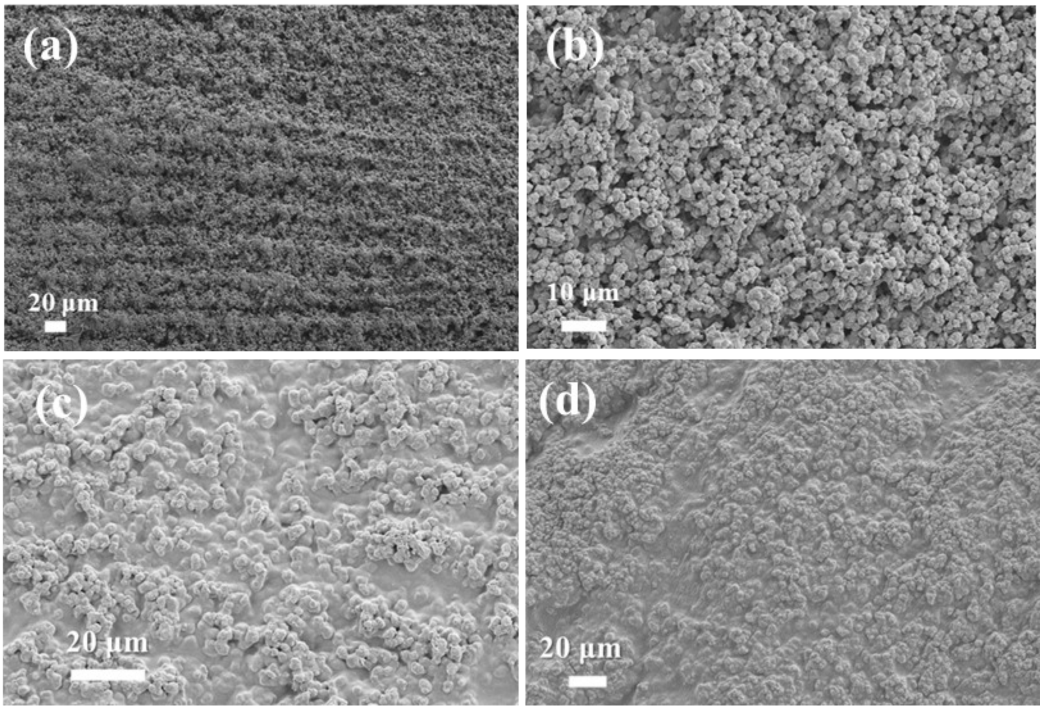

Fig. S16. SEM images of MOF-based cryogels after freeze-thaw cycling experiments. (a) UiO-66 cryogel; (b) AlFu cryogel; (c) MIL-91(Al) cryogel; (d) MIL-91(Ti) cryogel.

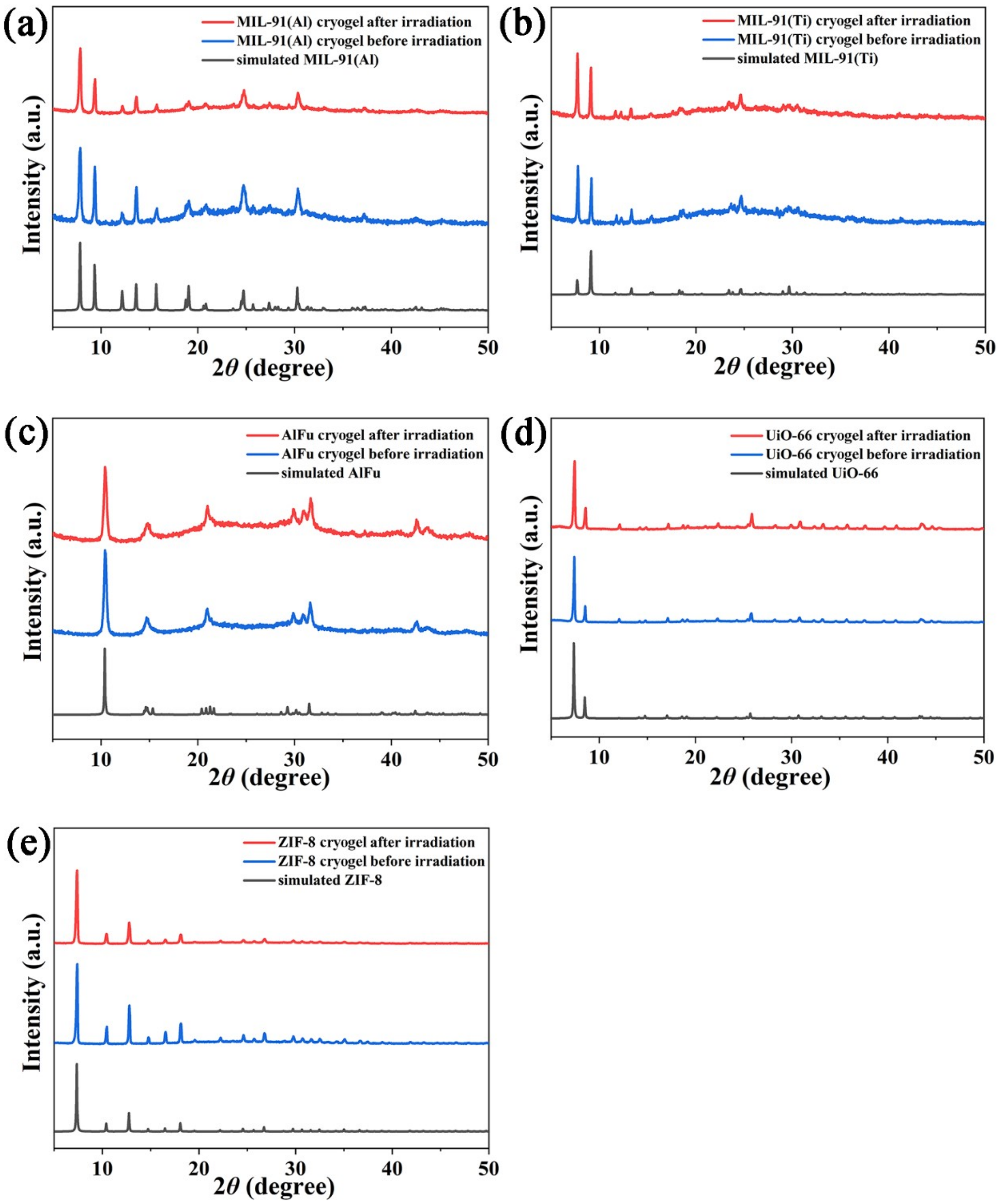

Fig. S17. XRD patterns of the MOFs-based cryogels treated with solar irradiation for 7 days. (a) MIL-91(Al) cryogel; (b) MIL-91(Ti) cryogel; (c) AlFu cryogel; (d) UiO-66 cryogel; (e) ZIF-8 cryogel.

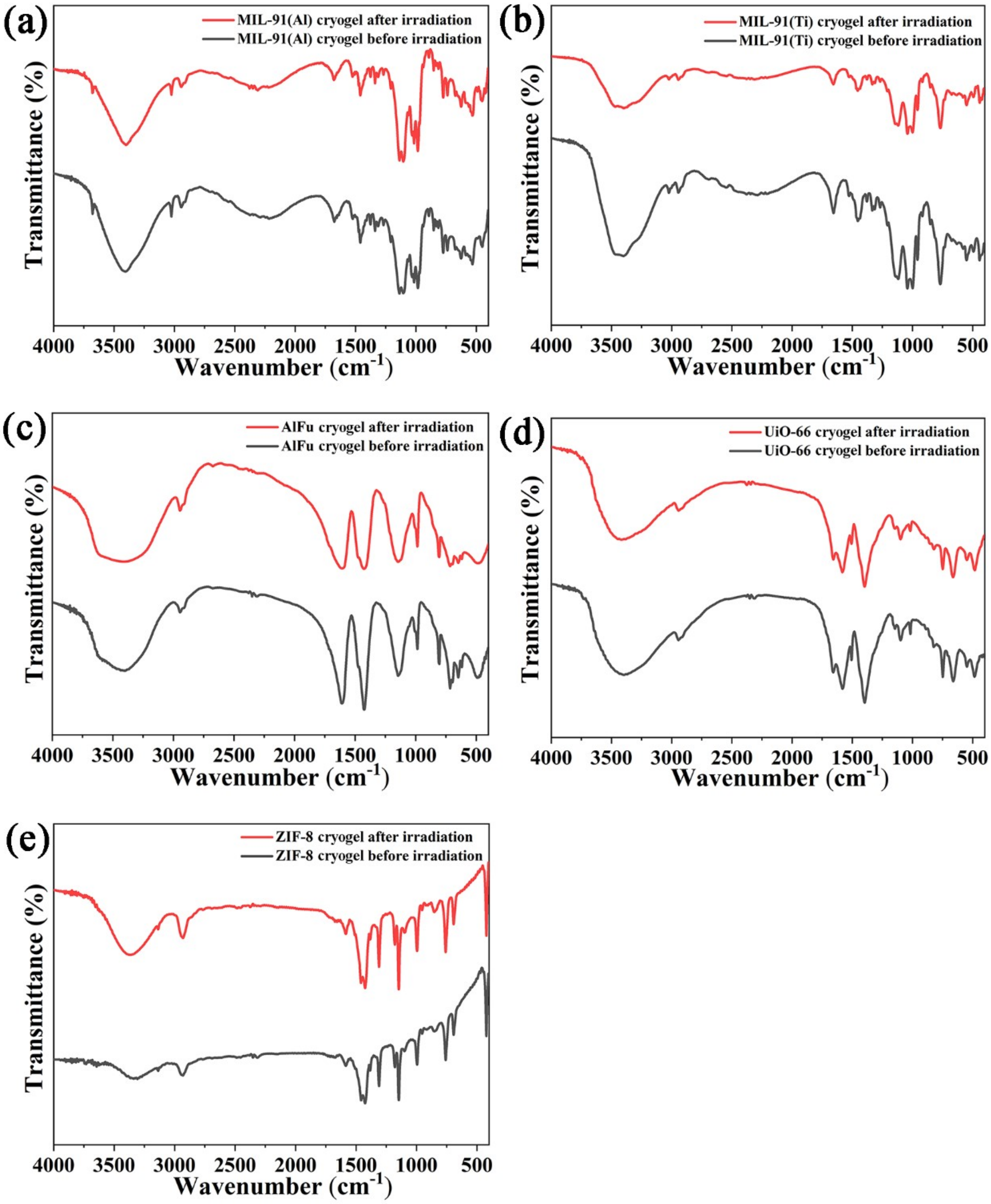

Fig. S18. FT-IR spectra of the MOFs-based cryogels treated with solar irradiation for 7 days. (a) MIL-91(Al) cryogel; (b) MIL-91(Ti) cryogel; (c) AlFu cryogel; (d) UiO-66 cryogel; (e) ZIF-8 cryogel.

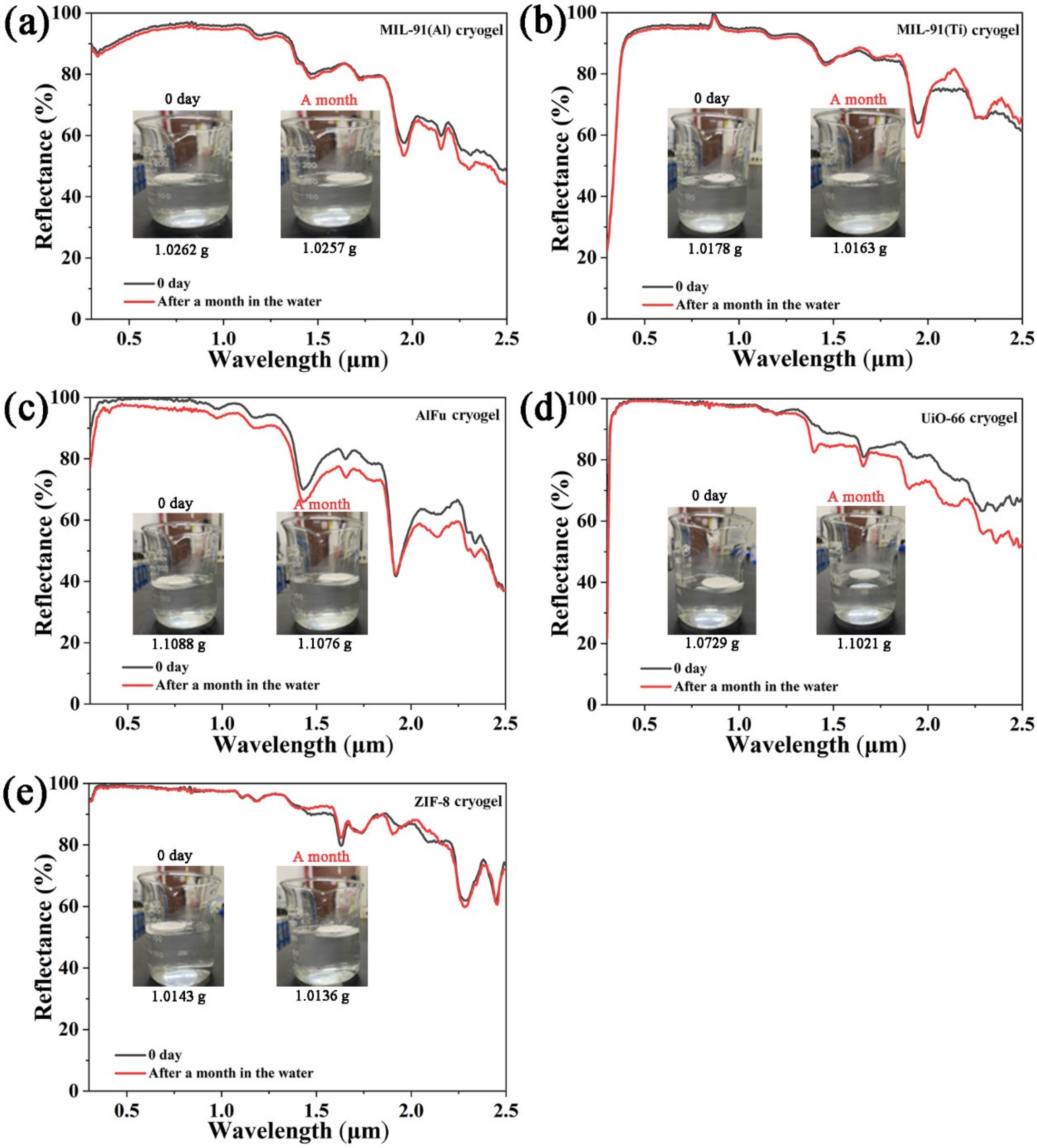

Fig. S19. The reflectance spectra of MOFs-based cryogels treated with water for a month (the insert images on the left and right show the sample immersing in water for 0 day and a month, respectively). (a) MIL-91(Al) cryogel; (b) MIL-91(Ti) cryogel; (c) AlFu cryogel; (d) UiO-66 cryogel; (e) ZIF-8 cryogel.

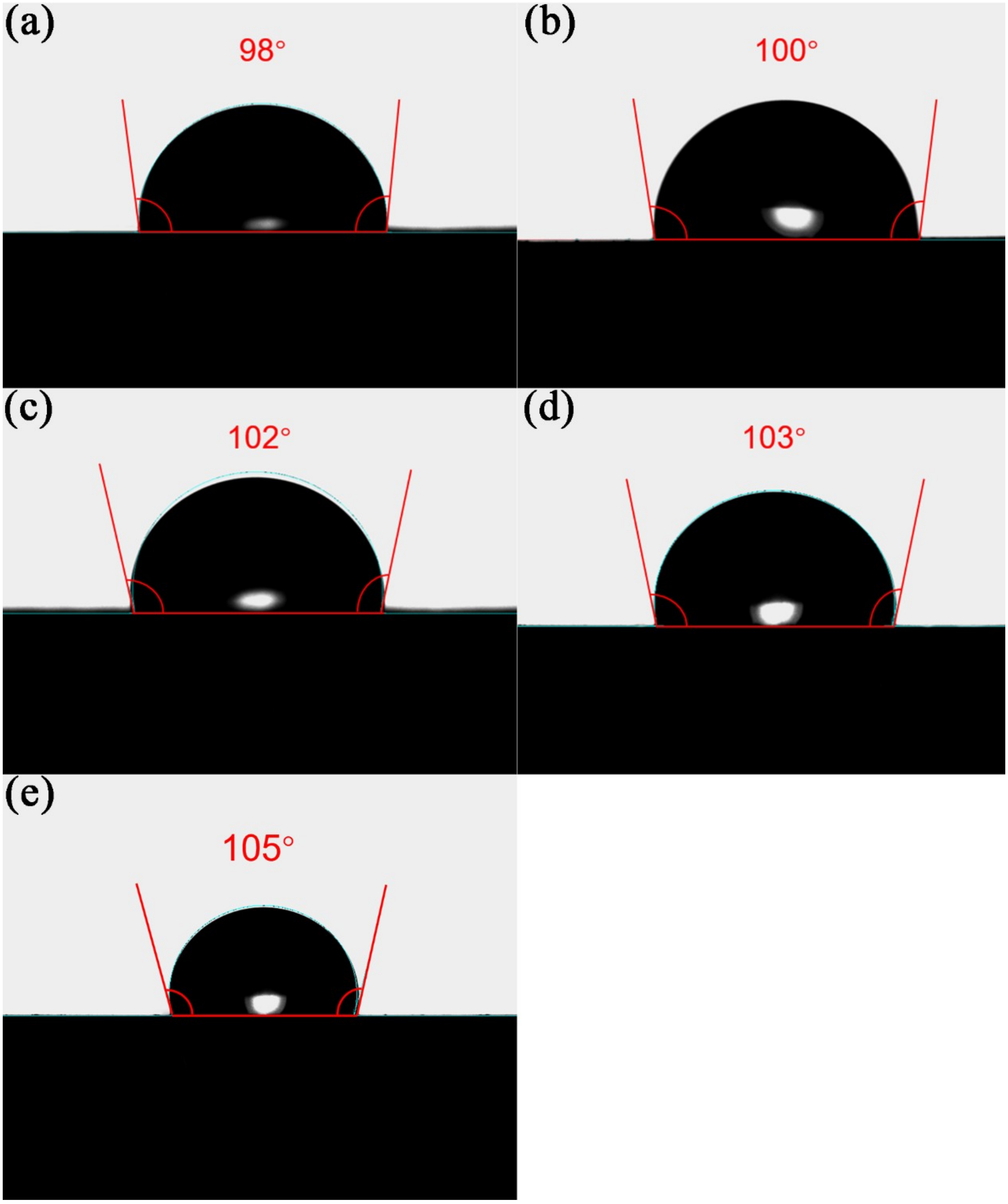

Fig. S20. The water contact angles of the MOFs-based cryogels. (a) MIL-91(Al) cryogel, (b) MIL-91(Ti) cryogel, (c) AlFu cryogel, (d) UiO-66 cryogel, (e) ZIF-8 cryogel.

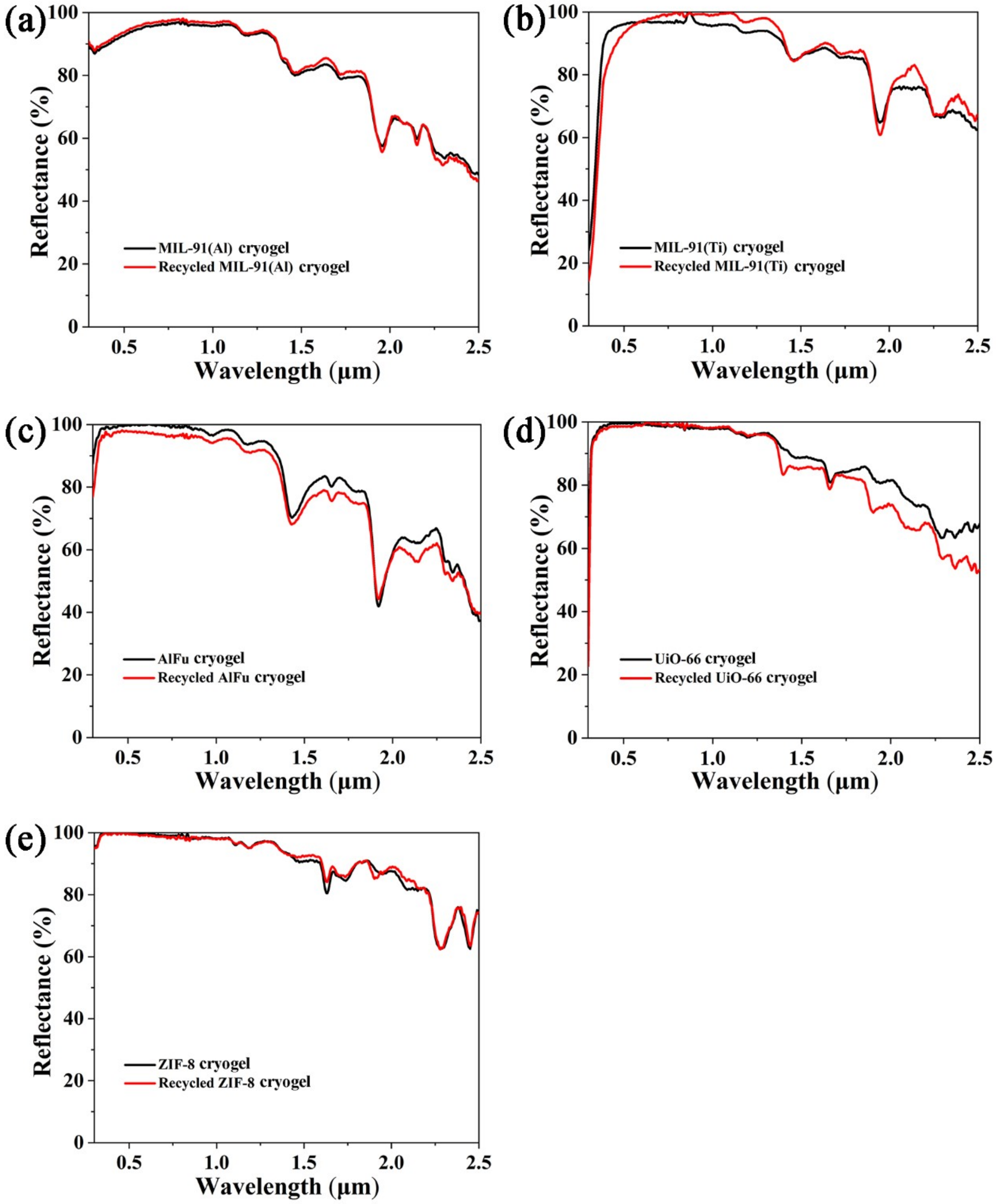

Fig. S21. Solar reflectance spectra of the MOF-based cryogels treated with utilization of recycling materials. (a) MIL-91(Al) cryogel; (b) MIL-91(Ti) cryogel; (c) AlFu cryogel; (d) UiO-66 cryogel; (e) ZIF-8 cryogel.

References

1 V. Benoit, R. S. Pillai, A. Orsi, P. Normand, H. Jobic, F. Nouar, P. Billemont, E. Bloch, S. Bourrelly, T. Devic, P. A. Wright, G. de Weireld, C. Serre, G. Maurin and P. L. Llewellyn, *J. Mater. Chem. A* 2016, **4**, 1383-1389.

2 Z. N. Kong, Z. D. Niu, L. He, Q. L. Chen, L. L. Zhou, Y. W. Cheng and Q. Q. Guan, *New J. Chem.*, 2018, **42**, 16985-16991.

3 K. Yang, Y. Li, Z. Zhao, Z. Tian and Y. Lai, *Chem. Eng. Res. Des.*, 2020, **153**, 562-571.

4 J. H. Cavka, S. Jakobsen, U. Olsbye, N. Guillou, C. Lamberti, S. Bordiga and K. P. Lillerud, *J. Am. Chem. Soc.*, 2008, **130**, 13850-13851.

5 M. Taheri and T. Tsuzuki, *ACS Mater. Lett.*, 2021, **3**, 255-260.

6 Z. Cheng, H. Han,F. Wang, Y, Yan, X. Shi, H. Liang, X, Zhang and Y. Shuai, *Nano Energy,* 2021, **89**, 106377.

7 D. Feng, A. S. Witty, F. I.Birnbaum Gonzalez, A.O. G. R. Felicelli, W.J. Lee, E. C. Barber and X. Ruan, *Adv. Mater.,* 2025, **37**, e04382.

8 Q. Cheng, C. Tang, B. W. Kim, Y. Xu, N. Yu, J. Mandal, H.Yin, Y. Yang, *Adv. Funct. Mater.,* 2025, **35***,* 2506405.

9 Y. Zhou J. Yang, X. Jia, J. Ni, N. Han and H. Song, *Prog. Org. Coat.,* 2024, **194**, 108631.

10 E. Zhang, C. Ma,T. Wang, L. Mu, Y. Yang and G. Chen. *Int. J. Biol. Macromol.,* 2025, **295**, 139580.

11 W. Jing, S. Zhang W. Zhang, Z. Chen, C. Zhang; D. Wu, Y. Gao and H. Zhu,. *ACS. Appl. Mater. Interfaces,* 2021, **13**, 29558-29566.

12 X. Y. Liu, P. L. Li, Y. J. Liu, C. Zhang, M. He, Z. T. Pei, J. Chen, K. M. Shi, F. Liu, W. L. Wang, W. Zhang, P. K. Jiang and X. Y. Huang. *Adv. Mater.,* 2024, **36** , 2409473.

13 A. J. Chang, C. H. Xue, J. J. Sun, J. Cheng, M. C. Huang, B. Y. Liu, H. D. Wang, X. J. Guo, C. Q. Ma, L. Wan, Y. G. Wu and Y. Y. Yan, *J. Mater. Chem. A,* 2025, **13**, 6440-6450.

14 Y. Fan, K. Feng, P. Xie, H. Tian, Y. Wu and F. Zhou, *Sustain. Mater. Technol.,* **2025**, *43*, e01334.

15 W. Cai, B. Lin, L. Qi, T. Cui, Z. Li, J. Wang, S. Li, C. Cao, M. Ziaur Rahman, X. Hu, R. Yu, S. Shi, W. Xing, Y. Hu, J. Zhu and B. Fei, *Chem. Eng. J.*, 2024, **488**, 150784

16 Q. R. Zhang, X. F. Wang, X. Y. Hu, D. H. Yang, H. L. Wei, X. Y. Cao, Y. B. Hou and J. Wang, *Compos. Commun.*, 2025, **57**, 102450

17 C. Q. Ma, C. H. Xue, W. Fan, X. J. Guo, J. Cheng, M. C. Huang, H. D. Wang, Y. G. Wu, B. Y. Liu and S. Q. Lv, *ACS Sustainable Chem. Eng.*, 2024, **12**, 5695−5704

18 A. J. Chang, C. H. Xue, J. J. Sun, J. Cheng, M. C. Huang, B. Y. Liu, H. D. Wang, X. J. Guo, C. Q. Ma, L. Wan, Y. G. Wu and Y. Y. Yan, *J. Mater. Chem. A*, 2025, **13**, 6440-6450

19 Y. N. Fan, J. H. Zhu, J. M. Li, X. Y. Liu, P. Liu, X. Jin, K. Y. Wang and L. F. Liu, *ACS Appl. Mater. Interfaces*, 2025, **17**, 34458-34469

20 M. Y. Liang, G. H. Xia, J. R. Lv, Y. W. Gong, Y. Wu, T. Wang and Y. N. Zhang, *Sol. Energy Mater. Sol. Cell.*, 2026, **296**, 114040

21 C. Y. Ren, Z. C. Wei, J. W. Wang, C. Y. Cai, B. Cai, Z. N. Wang and H. Lei, *Nano Energy*, 2025, **141**, 111076

22 S. N. Ouyang, Q. Jiang, Y. H. Wan, X. R. Qu, Z. C. Yu, H. L. He and J. F. Wang, *Int. J. Biol. Macromol.,* 2024, **275**, 133533

23 C. Yang, B. Cui, Y. Cui, J. Ding, X. Shu, W. Dai and W. Wang, *Chem. Eng. J.*, 2026, **530**, 173616